JOURNAL OF NATURAL PRODUCTS

pubs.acs.org/jnp

Article

High-Content Screening Pipeline for Natural Products Targeting Oncogenic Signaling in Melanoma

Lara Dürr,[‡] Tanja Hell,[‡] Maciej Dobrzyński, Alberto Mattei, Anika John, Nathanja Augsburger, Gloria Bradanini, Jakob K. Reinhardt, Florian Rossberg, Milos Drobnjakovic, Mahabir P. Gupta, Matthias Hamburger, Olivier Pertz, and Eliane Garo*

Cite This: *J. Nat. Prod.* 2022, 85, 1006−1017

Read Online

ACCESS | Metrics & More | Article Recommendations | Supporting Information

ABSTRACT: The incidence of melanoma, the most fatal dermatological cancer, has dramatically increased over the last few decades. Modern targeted therapy with kinase inhibitors induces potent clinical responses, but drug resistance quickly develops. Combination therapy improves treatment outcomes. Therefore, novel inhibitors targeting aberrant proliferative signaling in melanoma via the MAPK/ERK and PI3K/AKT pathways are urgently needed. Biosensors were combined that report on ERK/AKT activity with image-based high-content screening and HPLC-based activity profiling. An in-house library of 2576 plant extracts was screened on two melanoma cell lines with different oncogenic mutations leading to pathological ERK/AKT activity. Out of 140 plant extract hits, 44 were selected for HPLC activity profiling. Active thymol derivatives and piperamides from *Arnica montana* and *Piper nigrum* were identified that inhibited pathological ERK and/or AKT activity. The pipeline used enabled an efficient identification of natural products targeting oncogenic signaling in melanoma.

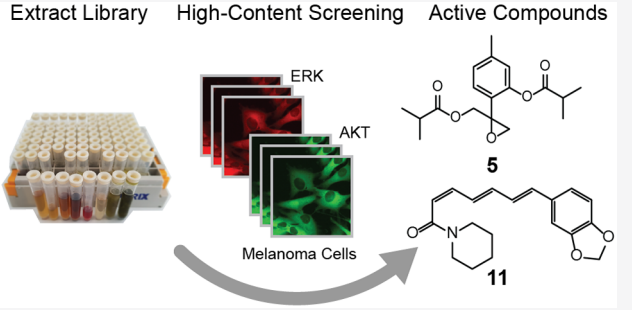

The incidence of melanoma, the most fatal dermatological cancer, has increased dramatically over the last several decades.[1] Frequent mutations are found in the MAPK/ERK (mitogen-activated protein kinase/extracellular signal-regulated kinase) and PI3K/AKT (phosphoinositide 3-kinase/AK strain transforming kinase) pathways, which are involved in the proliferation and in the survival and regulation of metabolism (Figure S1, Supporting Information).[2] In approximately 50% of all metastatic melanoma cases, an activating *BRAF* (v-raf murine sarcoma viral oncogene homologue B1) V600 mutation is found. This mutation drives aberrant MAPK/ERK pathway activation and tumor progression. To date, three drugs targeting BRAF V600, namely, vemurafenib, dabrafenib, and encorafenib, have been approved by the U.S. FDA. These agents show significant benefits regarding overall survival, progression-free survival, and promising overall response rates. Nevertheless, about 50% of patients relapse within the first 6−8 months of drug therapy due to drug resistance, leading to reactivation of the MAPK/ERK pathway, and the median overall survival is 14 months.[3,4]

Another critical signaling pathway regulating survival, apoptosis, and growth is the PI3K/AKT pathway. It is activated in over 20% of relapsed patients and, therefore, is an additional promising target in melanoma.[5,6] PTEN (phosphatase and tensin homologue deleted on chromosome 10) is the main negative regulator of PI3K, and loss of PTEN function leads to constitutive AKT activation. Loss of function of *PTEN* is observed in 10−30% of malignant melanomas. Mutation of the small GTPase NRAS (NRAS Q61K mutation), in addition to impacting ERK, also leads to constitutive activation of PI3Ks, leading to AKT activity.[7] There are, however, no PI3K-AKT inhibitors used currently in the clinical treatment of melanoma.[8]

One strategy to overcome these types of drug resistances involves the use of combination therapies. Combinations of BRAF and MEK (mitogen-activated protein kinase) inhibitors indeed have shown increased clinical response rates and improved progression-free and overall survival.[9] Combination therapy has thus become the standard treatment for advanced-stage melanoma patients harboring *BRAF* V600 mutations.[10] Moreover, as both the MAPK/ERK and PI3K/AKT pathways can be mutated and contribute to oncogenic proliferation and survival, targeting both pathways simultaneously represents a promising therapeutic strategy. Preclinical success on cancer cell lines and tumor xenografts has already led to several

Received: December 7, 2021
Published: March 1, 2022

Downloaded via UNIV OF BASEL on April 25, 2022 at 11:10:55 (UTC).
See https://pubs.acs.org/sharingguidelines for options on how to legitimately share published articles.

ACS Publications

© 2022 American Chemical Society and American Society of Pharmacognosy

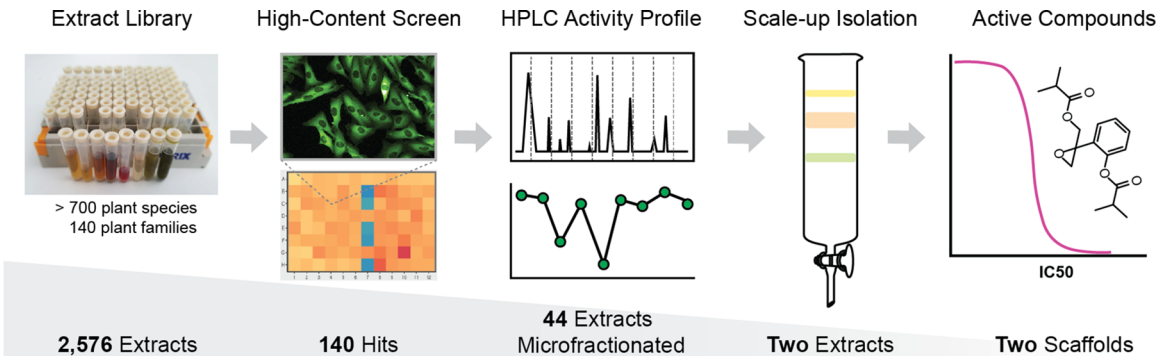

Figure 1. Overview of the screening pipeline. A total of 2576 plant extracts from 140 different plant families were screened with the HCS assay. Of the 140 hits, the 44 most promising extracts were submitted to HPLC-based activity profiling. Scale-up work on two extracts led to the isolation of 12 compounds belonging to two different scaffolds.

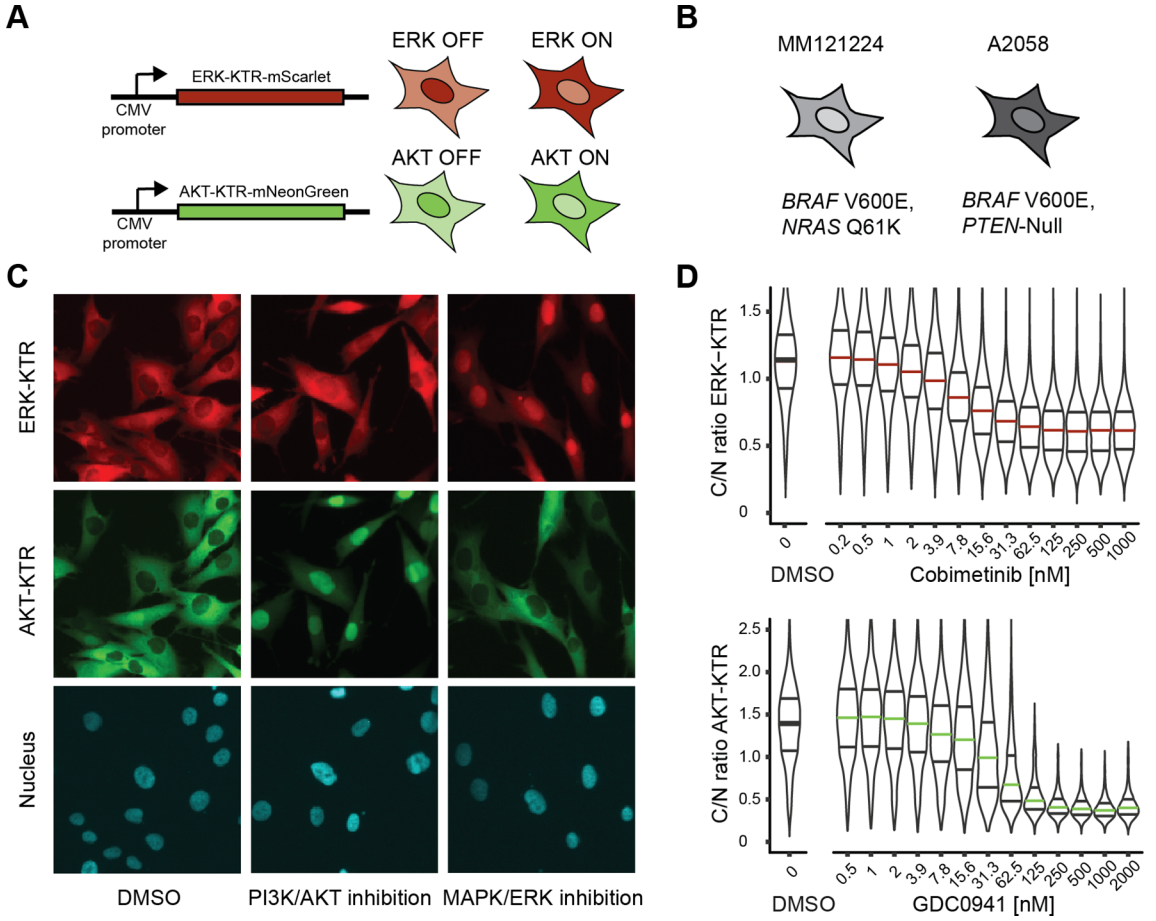

Figure 2. Principle of the biosensors used in the HCS. (A) Schematic representation of the genetically encoded biosensors (KTRs) with their fluorophores (mScarlet and mNeoGreen) used for assay readout. (B) Schematic representation of MM121224 and A2058 cell lines and their mutations. (C) Representative images of MM121224 cells expressing the different biosensors (ERK-KTR in red, AKT-KTR in green, and histone H2B for nucleus in turquoise) are shown under treatment with two positive controls, the MEK inhibitor cobimetinib (leading to ERK inhibition) and the PI3K inhibitor GDC0941 (leading to AKT inhibition) and with a negative control (DMSO control). (D) Concentration−response curves of cobimetinib and GDC0941 on ERK and AKT activity in the MM121224 cell line. The cytoplasm to nucleus ratio fluorescence intensity (C/N ratio) was used as a measure of pathway inhibition. Data distributions from single cells are represented as violin plots; median of treatment distribution (middle bar) and first and third quartiles are shown. Data are taken from at least 200 cells.

clinical studies of combination therapies targeting the two pathways. Unfortunately, however, the few trials that were conducted have revealed poor tolerability of these combinations, precluding optimal therapeutic dosing.[11] In contrast, preclinical studies with dual AKT/ERK inhibitors, such as ONC201, have shown promising results.[12] There is therefore no doubt that novel compounds targeting oncogenic MAPK/ERK and PI3K/AKT signaling in melanoma would add to the drug arsenal for combination therapy.

Identifying new MAPK/ERK and PI3K/AKT pathway inhibitors may involve either a target-based or a phenotype-based approach. The target-based approach starts with a

https://doi.org/10.1021/acs.jnatprod.1c01154
J. Nat. Prod. 2022, 85, 1006−1017

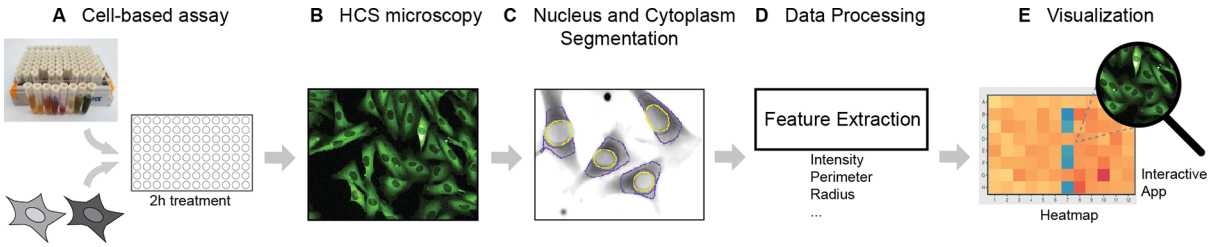

Figure 3. Workflow in the HCS, data analysis, and visualization. (A) Cells were treated with extracts in a 96-well plate format. (B) Automated HCS microscopy was used for image acquisition. (C) Each cell was segmented into the nucleus (shown in yellow) and the cytosol (shown in purple), and median pixel intensities were quantified in the cytoplasm and nucleus to obtain the C/N ratio. (D) Cells with unusual morphology were identified using a machine-learning random forest model based on cell geometric features and were excluded from data analysis. (E) Results were visualized as heatmaps using an interactive app that allowed for rapid quality control of the primary data.

defined molecular target that is assumed to impact the disease. In the case of melanoma, BRAF V600E was validated as a target by different in vitro and in vivo studies.[13−17] A fragment-based screening on several kinases, followed by cocrystallographic screening with BRAF, led to the discovery of vemurafenib.[18] In principle, it would be possible to perform similar approaches for all possible targets in the MAPK/ERK and PI3K/AKT pathways. However, this would require a significant effort and high costs. In contrast, phenotypic screens typically measure alterations in cell properties such as morphology, levels of various proteins, or functional properties such as cell proliferation. A major challenge then consists in the identification of the target and its mechanism of action. Herein were used genetically encoded biosensors based on kinase translocation reporter (KTR) technology that report on ERK and AKT kinase activity directly in single cells.[19] This enables compounds to be identified that target proteins in pathways induced by oncogenic mutations. Identification of compounds operating directly within living cells can take into account the robustness of signaling networks leading to tumor adaptation and resistance.[20,21]

Translating this biosensor technology to a medium-throughput high-content screen (HCS) format enabled the efficient screening of a large plant extract library, and subsequent HPLC activity profiling was used to select the most promising extracts for targeted isolation (Figure 1).[22] The approach taken is illustrated by isolation of bioactive compounds from *Arnica montana* L. (Asteraceae) and *Piper nigrum* L. (Piperaceae).

RESULTS AND DISCUSSION

HCS Assay Development. To measure simultaneously ERK and AKT activity in single cells, cell lines were produced stably expressing ERK-KTR fused to an mScarlett fluorophore[23] and AKT-KTR consisting of a mutated forkhead box protein 1 allele fused to an mNeonGreen fluorophore[24] (Figure 2A). These spectrally compatible biosensors measure ERK and AKT activity depending on their cytosolic (ON state) versus nuclear (OFF state) localizations. Two different melanoma cell lines expressing both biosensors were produced. The A2058 human melanoma cell line harbors the classical *BRAF* V600E mutation leading to constitutive ERK activation, as well as a *PTEN* deletion, producing PI3K and subsequent AKT activation. The MM121224 patient-derived cell line also harbors the *BRAF* V600E mutation, but bears an additional *NRAS* Q61K mutation that leads to elevated PI3K/AKT signaling (Figure 2B).[25] It must be noted that the MM121224 line originated from a patient with a primary *BRAF* V600E mutation, whose cells acquired a second *NRAS* Q61K mutation in response to BRAF inhibition targeted therapy.[26] This cell line therefore represents a model for genetic drug resistance. Thus, both cell lines exhibit high ERK and AKT activity, with the elevated AKT activity emerging through different mechanisms due to different oncogenes.

Imaging of ERK and AKT-KTR revealed prominent cytosolic fluorescence indicating high ERK/AKT activity in MM121224 cells (Figure 2C). The nuclei were visualized using a histone H2B-mTurquoise fusion protein (while A2058 cells were DAPI stained). The high brightness of the biosensor system permitted measurements using 10× air objectives compatible with a high-content screening microscope. Treatment with the ERK pathway inhibitor cobimetinib led to the inhibition of ERK activity as documented by nuclear ERK-KTR relocalization (Figure 2C), without any effect on AKT activity. In turn, treatment with the PI3K-specific inhibitor GDC0941 led to AKT inhibition without any effect on ERK activity. These results showed that the two biosensors specifically report on elevated ERK and AKT activities in the MM121224 cell line.

To quantify the ERK and AKT activities, an image analysis workflow was established in which each cell nucleus in an image was segmented. The nuclei were used to derive two regions of interest: a nucleus mask and a cytosol mask that consists of a ring of a specific width around the nucleus and that is contained within the cytosol (Figure 3C). The ratios of the median pixel values of the cytosolic over the nuclear mask (C/N ratio) were calculated. Thus, high C/N ratios are indicative of high ERK/AKT activities (and vice versa). The functionality of the biosensors was confirmed with the known inhibitors cobimetinib and GDC0941 via a concentration-dependent response of ERK and AKT activities (Figure 2D). Similar results were observed in A2058 cells with cobimetinib and AZD5363 (Figure S2, Supporting Information). These data confirm that ERK and AKT-KTR biosensors quantitatively and specifically measure ERK and AKT activities in single cells.

Next, the biosensor assay was adapted for high-content screening of the available plant extract library. The different steps of the experimental/computational workflow are depicted in Figure 3. Cells were plated at subconfluent density in 96-well plates, providing sufficient cell measurements for robust statistics. A treatment duration of 2 h with plant extracts was chosen to avoid potential cytotoxicity that might hamper the biosensor measurements owing to cell morphology changes. This experimental modality was also more likely to measure a direct impact on MAPK/ERK and PI3K/AKT

https://doi.org/10.1021/acs.jnatprod.1c01154
J. Nat. Prod. 2022, 85, 1006−1017

signaling before potential long-term adaptation due to transcriptional rewiring of signaling pathways occurs.[27,28]

Since the extract library used DMSO as a solvent, the DMSO tolerance was determined for both cell lines. Fluorescence signals and cell health were not affected at DMSO concentrations of ≤0.75% (data not shown). Given a 10 mg/mL concentration of library stock solutions, the highest extract concentration to be tested was 75 μg/mL. All extracts were screened in duplicate. Images were acquired in fixed cells for ERK-KTR, AKT-KTR, and nuclei using a high-content microscopy platform (Figure 3B). Single-cell ERK and AKT-KTR C/N fluorescence ratios were extracted using an automated image analysis pipeline (Figure 3C).

A major challenge of data analysis was to identify dying cells affected by cytotoxic samples. These cells differ from healthy cells since they are small and round, which prevents extraction of a meaningful C/N ratio (C/N ratio very low), leading to false-positive results. To improve the accuracy of the image analysis pipeline used, cells affected by cytotoxicity were manually annotated based on their distinctive round shape. These annotations then were used to train a random forest model to recognize round cells and abnormally high mean fluorescence intensity to exclude them from analysis (Figure 3D).

To normalize plate-to-plate variations, the C/N ratio was rescaled into the normalized percentage of inhibition (NPI) or the *z*-score (the standard score). The NPI is the inhibition relative to negative and positive controls, while the *z*-score is the number of standard deviations a sample differs from the mean of all wells in the screening plate except of control wells. Finally, an interactive web portal was developed to browse original images and visualize their activity in a plate map. This enabled a rapid visual quality control of the hits (Figures 3E and S3, Supporting Information).

Library Screening. An in-house library of 2576 extracts from 140 different plant families and over 700 species was screened.[22] Given that the activity of two signaling pathways (MAPK/ERK and PI3K/AKT) in two different cell lines was measured, four lists were generated. Extracts in these lists were ranked according to the *z*-score or the NPI value. The threshold for hits was established by a visual examination of the 100 highest ranked extracts, except for AKT activity in MM121224 cells, in which the 200 highest ranked extracts were taken into consideration. In A2058 cells, the threshold (*z*-score) for ERK activity was set empirically to −1.3 for ERK activity and −1.9 for AKT activity (*z*-score). In MM121224 cells, the threshold (NPI) was set to 0.68 for ERK activity and to 0.56 for AKT activity. This led to a total of 140 hits (Tables S1−S4, Supporting Information).

A significantly higher number of hits was observed for AKT (121 in MM121224 cells and 35 in A2058 cells) than for ERK activity (five hits with each cell line) (Figure 4). This suggests that the PI3K/AKT pathway is more "druggable" than the MAPK/ERK pathway. Recent studies have shown that the MAPK pathway is wired to be robust against perturbations of its components, possibly explaining why so few compounds can lead to ERK inhibition in cells with a *BRAF* V600E mutation.[28−30] A kinome siRNA screen performed on MM121224 cells has also shown that a much smaller number of kinases had an effect on ERK versus AKT activity using the same biosensor system.[25] A significantly higher number of AKT hits was observed with MM121224 cells (121 hits) when compared to A2058 cells (35 hits) (Figure 4C). This may be

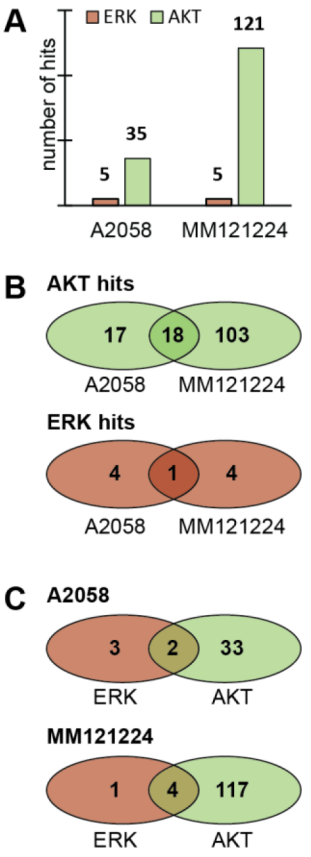

Figure 4. (A) Hit distribution in A2058 and MM121224 cell lines and on their two biosensors. (B) Venn diagram showing ERK and AKT hit distribution between cell lines. (C) Venn diagram showing hit distribution on A2058 and MM121224 cells.

explained by different mutations (Figure S1, Supporting Information). In A2058 cells, a lack of PTEN lipid phosphatase activity led to increased phosphatidylinositol (3,4,5)-triphosphate (PIP3) and, thus, increased PI3K/AKT signaling, while in MM121224 cells, the presence of an *NRAS* Q61K mutation led to Ras-dependent PI3K activation. *PTEN* deletions might be more difficult to target than an *NRAS* mutation since the protein is absent. These results suggest strongly that different oncogenic mutations that converge on the same signaling pathway (here AKT) will require inhibition of different targets of the signaling cascade using distinct sets of compounds. The present screening strategy was well suited to accommodate this need.

HPLC-Based Activity Profiling and Selection of Extracts for Isolation. The extracts were selected for microfractionation based on their potency in the HCS and the taxonomic classification of their corresponding plant families. In this manner, a set of 44 extracts was submitted to the HPLC-based activity profiling approach used routinely in the laboratory.[22] Out of 44 extracts, 37 extracts still displayed inhibition of the MAPK/ERK and/or PI3K/AKT pathway when fractionated.

The selection of extracts for scale-up isolation was based on the activity profile obtained, the taxonomy of the plant family or genus, a literature search (dereplication of peaks present in active windows), and the availability of sufficient plant material. The petroleum ether (PE)/EtOAc library extracts from the plants *A. montana* and *P. nigrum* showed promising inhibition of ERK and/or AKT activity on both cell lines in the

https://doi.org/10.1021/acs.jnatprod.1c01154
J. Nat. Prod. 2022, 85, 1006−1017

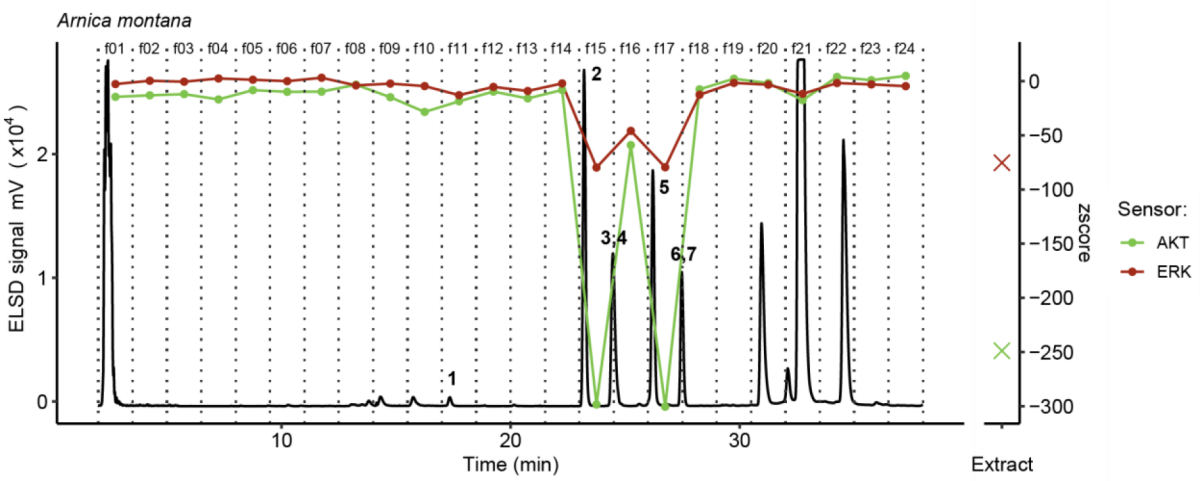

Figure 5. HPLC-based activity profile of a fresh scale-up EtOAc extract of *Arnica montana* (AMR-SU) with the A2058 cell line. The activity of AKT and ERK is shown in green and red, respectively, while the activity of the crude extract is presented to the right as a cross. Bold numbers refer to isolated compounds **1**−**7**. For both ERK and AKT activity, two windows of activity are seen in fractions 15 and 17.

primary screen, as well as promising activity in the microfractions (Figure 7, Tables S1−S4, Figure S4, Supporting Information). The library PE extract of *A. montana* roots (AMR-LE) was the only hit showing ERK inhibition on both cell lines. Moreover, the peaks present in the activity windows of the activity profile (Figure S4, Supporting Information) did not correspond to any well-known secondary metabolite in this species. This extract was therefore selected for scale-up work.

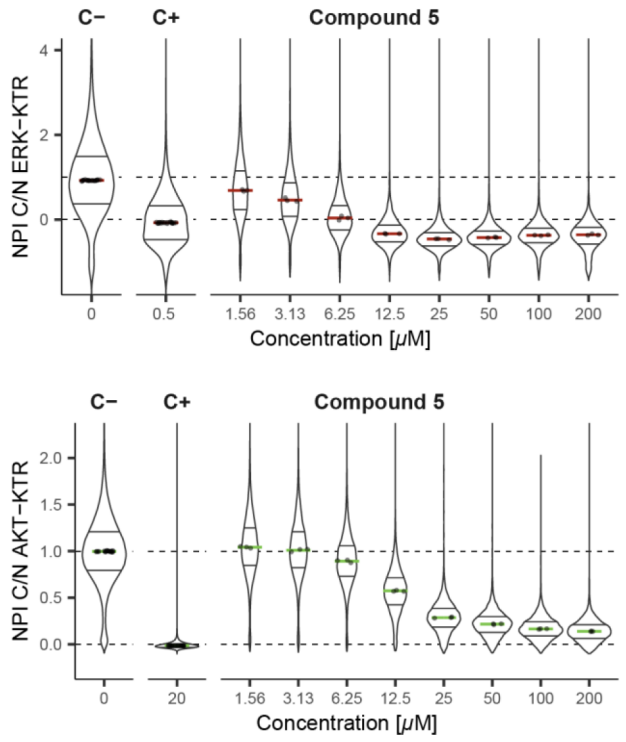

Figure 6. Concentration−response curve for compound **5** on ERK and AKT activity in A2058 cells. C+ and C− designate positive (20 μM AZD5363 as AKT inhibitor and 500 nM cobimetinib as MAPK/ERK pathway inhibitor) and negative (0.75% DMSO) controls. Data distributions from single cells are represented as violin plots; median of treatment distribution (middle bar) and first and third quartiles are shown. Data are taken from at least 200 cells.

The extract of *P. nigrum* was of interest due to the activity profile obtained with the MM121224 cell line (Figure 7). Thus, it was therefore decided to further study this extract as well.

Arnica montana. A scale-up EtOAc extract of *A. montana* roots (AMR-SU) was prepared from plant material purchased in 2019. As shown in Figure S4 (Supporting Information), the HPLC chromatogram differed somewhat from the library extract AMR-LE, and a new activity profile of AMR-SU therefore was generated based on activity data obtained with the A2058 cell line (Figure 5). The preparative isolation of these compounds was commenced 15 months later, in January 2021. At that time, the AMR-SU extract was analyzed again, and after storage for 15 months at −20 °C, surprisingly the extract composition had changed. Interestingly, the chromatogram of AMR-SU done in 2021 was similar again to the library extract AMR-LE. Peaks corresponding to compounds **5**−**7** were detected only in the extract that was freshly prepared and were detected neither in the library extract AMR-LE nor in the scale-up extract AMR-SU analyzed after 15 months (Figure S6, Supporting Information). As both the library and the scale-up extract were stored at −80 and −20 °C, respectively, this suggested the degradation of **5**−**7** occurred even at low temperatures. The activity profile obtained with the AMR-SU extract displayed two main active fractions, namely, f15 and f17 (Figure 5).

Compounds **1**−**7** were obtained as colorless, oily substances. Their structures were identified based on the ^{1}H and 2D NMR spectra as thymol derivatives **1**−**7**.[31−35] Electronic circular dichroism (ECD) spectra and optical rotation data suggested the presence of mixtures of enantiomers (Figures S21, S23, S25, S27, S29, Supporting Information). An attempt to determine the enantiomeric access in natural epoxythymols using a published BINOL methodology was not successful.[36] Compounds **2**, **5**, **6**, and **7** have been reported previously from the roots of *A. montana*, and **5**−**7** were only obtained as a mixture.[37]

Migration of acyl moieties appears to be responsible for the degradation of epoxides **5**−**7** to **2**−**4**. Even though acyl migration has not been reported in thymol derivatives, it has been shown to occur in other natural products such as aescin

https://doi.org/10.1021/acs.jnatprod.1c01154
J. Nat. Prod. 2022, 85, 1006−1017

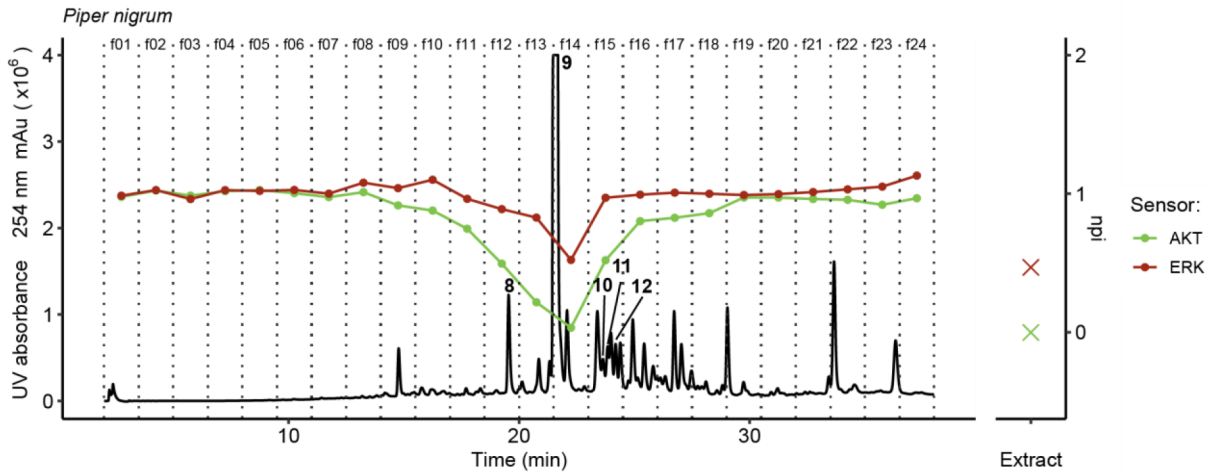

Figure 7. HPLC-based activity profile of an EtOAc extract of *Piper nigrum* fruits with the MM121224 cell line. The normalized percentages of inhibition of AKT and ERK are shown in green and red, respectively, and inhibition of the extract is presented to the right. Bold numbers refer to isolated compounds **8**−**12**.

Chart 1

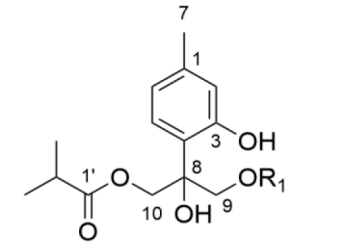

1 R_1 = H
2 R_1 = isobutanoyl
3 R_1 = 2-methylbutanoyl
4 R_1 = isopentanoyl

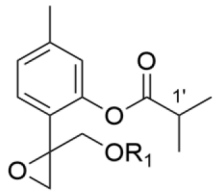

5 R_1 = isobutanoyl
6 R_1 = 2-methylbutanoyl
7 R_1 = isopentanoyl

and coumarins.[38,39] A putative mechanism is proposed (Scheme 1, Supporting Information).

While all compounds displayed micromolar activity on both pathways, epoxides **5**−**7** showed slightly greater inhibition potencies than **1**−**4** (Table 1 and Figures S31−S34, Supporting Information). Compound **5** showed the highest activity on A2058 cells, with IC_{50} values of 11.8 ± 0.5 and 4.7 ± 0.6 μM for AKT and ERK, respectively (Figure 6). The PI3K/AKT pathway inhibition of all compounds was greater in A2058 cells than in MM121224 cells. This was surprising since PI3K/AKT signaling seems to be more druggable in MM121224 than in A2058 cells, as discussed above. Understanding the mechanism of action of these compounds might therefore be of great interest to inhibit high PI3K/AKT signaling in response to a *PTEN* deletion.

Table 1. Activities of Compounds 1−7 on AKT and ERK in A2058 and MM121224 Cells

	IC_{50} value in A2058 [μM]		IC_{50} value in MM121224 [μM]	
compound	AKT	ERK	AKT	ERK
1	66.4 ± 3.8	34.2 ± 2.4	>100[a]	>100[a]
2	92.9 ± 18.4	43.6 ± 8.6	>100[a]	>100[a]
3	49.6 ± 2.6	25.3 ± 1.7	>100[a]	>100[a]
4	71.2 ± 6.7	34.4 ± 2.8	>100[a]	>100[a]
5	11.8 ± 0.5	4.7 ± 0.6	35.4 ± 3.7	24.9 ± 2.2
6	31.9 ± 3.0	12.9 ± 0.9	>100[a]	>100[a]
7	20.6 ± 1.8	9.1 ± 0.9	67.6 ± 8.2	50.7 ± 7.7

[a]IC_{50} values could not be determined since a 100% inhibition was not reached at 200 μM.

Thymol was recently shown to downregulate both PI3K/AKT and MAPK/ERK pathways, albeit with a long incubation time (24 h) and very high concentrations (0.5−2 mM).[40] In contrast, the thymol derivatives obtained in the present investigation inhibited the MAPK/ERK and PI3K/AKT pathways already after 2 h. This suggests strongly that they specifically inhibited oncogenic MAPK/ERK and PI3K/AKT activity.

To confirm the results from the image-based HCS read-out, immunostaining in MM121224 cells with anti-phospho-ERK and -phospho-AKT on serine 473 antibodies was performed with compounds **1**, **3**, and **5** (Figure S35, Supporting Information). Inhibition of AKT was confirmed, but, unexpectedly, a concentration-dependent increase of phospho-ERK levels was observed. An explanation for this seemingly paradoxical finding may be that the phospho-ERK antibody reveals the phosphorylation by the MAP2K MEK, and thus ERK activation, while the ERK-KTR measures the catalytic activity of ERK. As ERK exhibits negative feedback regulation to MAP3K RAF and MAP2K MEK, a direct inhibition of ERK catalytic activity might switch off the negative feedback and, thereby, lead to increased Raf and MEK activity and ERK phosphorylation (Figure S1, Supporting Information).[41] These results, therefore, suggest strongly that the purified thymol derivatives directly target the catalytic

https://doi.org/10.1021/acs.jnatprod.1c01154
J. Nat. Prod. 2022, 85, 1006−1017

activity of ERK. As these compounds simultaneously target both the MAPK/ERK and PI3K/AKT pathways, an exact understanding of their mode of action might allow these scaffolds to be used as an inspiration for the development of dual inhibitors of the MAPK/ERK and PI3K/AKT pathways.

Piper nigrum. The HPLC activity profile of the EtOAc extract with MM121224 cells displayed a broad activity window with f14 being the most active fraction (Figure 7). However, the corresponding time window in the HPLC-UV trace displayed several peaks, among them the dominant peak of piperine (**9**). Therefore, an optimized separation by semipreparative HPLC was used to enable a peak-based fractionation of compounds.[42] All peaks were collected as fractions and tested in MM121224 cells (Figure S38, Supporting Information) at a concentration of 75 μg/mL. Four of these displayed AKT activity (Figure S38, Table S7, Supporting Information). Subsequently, a large scale-up procedure was performed, which led to the isolation and identification of trichostachine (piperyline) (**8**),[43,44] 6,7-dehydrobrachyamide B (**10**),[44,45] (2*Z*,4*E*,6*E*)-piperettine (**11**),[46] and piperolein A (**12**).[47] Piperine (**9**) was confirmed by comparison with an authentic reference.

Chart 2

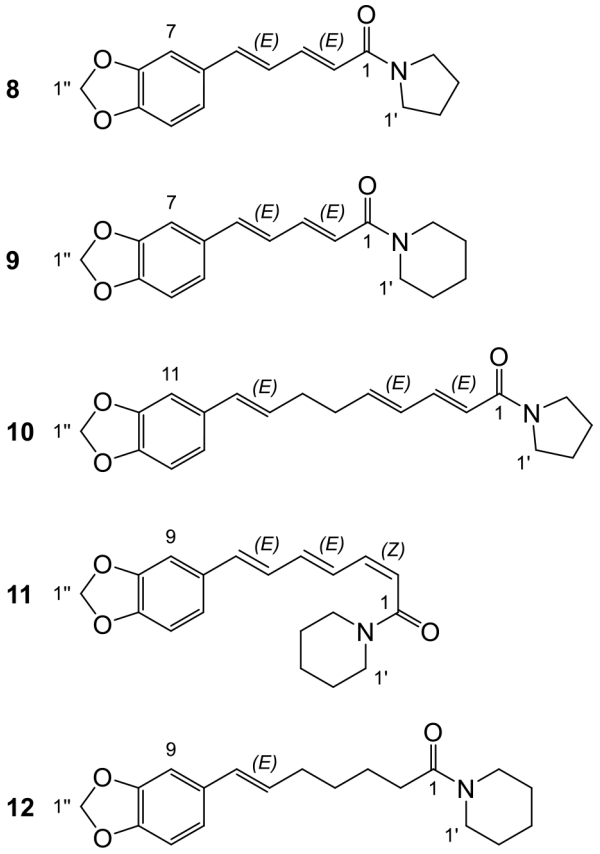

Concentration responses indicated compound **10** to be the most potent piperamide active on both cell lines (Figures 8 and S51, Supporting Information). Visual examination indeed confirmed this compound to be most active on AKT in MM121224. A clear IC_{50} could not be determined, as the plateau was not reached at 200 μM. However, a visual control suggests compound **10** to be cytotoxic for A2058 cells, which

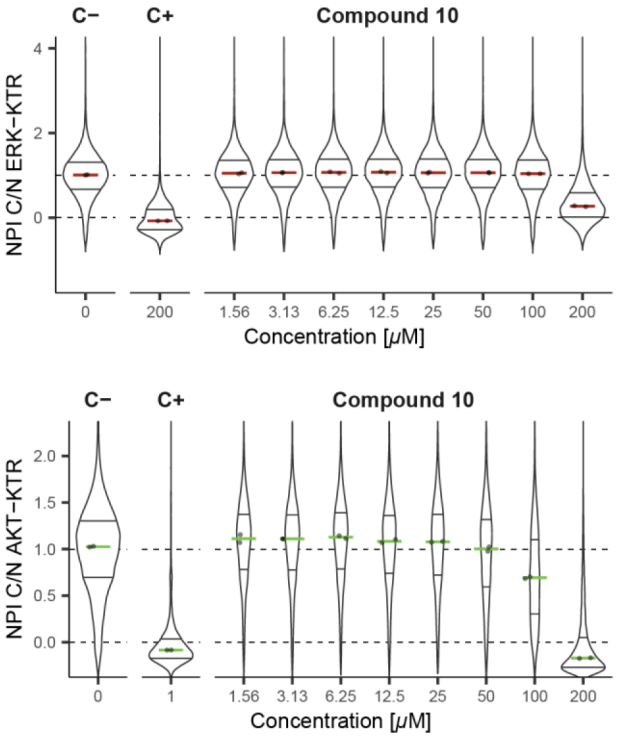

Figure 8. Concentration−response curve for compound **10** on ERK and AKT activity in MM121224 cells. C+ and C− designate positive (1 μM GDC0941 as PI3K/AKT pathway inhibitor; 200 nM cobimetinib as MAPK/ERK pathway inhibitor) and negative (0.75% DMSO) controls. Data distributions from single cells are represented as violin plots; median of treatment distribution (middle bar) and first and third quartiles are shown. Data are taken from at least 200 cells.

explains the violin shapes observed for AKT and ERK activity at 200 μM.

Piperamides **8**, **11**, and **12** inhibited the PI3K/AKT pathway at 200 μM only in the MM121224 cell line. Piperine (**9**) only inhibited AKT to some extent on this cell line and thus was the least active compound (Figure S53, Supporting Information). Interestingly, piperine has been shown to decrease phosphorylated ERK and AKT in different cancer cells, in a similar concentration range to that used in the present experiments (150−160 μM), but with significantly longer exposure.[48,49] In both cell lines, piperolein A (**12**) displayed weak ERK inhibition at 200 μM. Compounds **8** and **9** were not active on the ERK biosensor (Figure S52, Supporting Information). The piperamide **11** was only active against MAPK/ERK in MM121224 cells.

The activity measured by the biosensor was confirmed by immunostaining experiments in MM121224 cells for phosphorylated ERK and AKT (Figure S54, Supporting Information). Cells treated with compound **10** showed a concentration-dependent decrease in phosphorylated AKT and phosphorylated ERK at 200 μM, while compounds **11** and **12** showed only a marginal or no effect for the two kinases.

CONCLUSIONS

The present HCS-based discovery pipeline combining multiplexed measurement of ERK and AKT activity in single cells and HPLC-based activity profiling enabled a rapid and cost-effective screening of a library comprising 2576 extracts. The KTR-based technology applied herein using a medium-

https://doi.org/10.1021/acs.jnatprod.1c01154
J. Nat. Prod. 2022, 85, 1006−1017

throughput mode HCS is potentially applicable to other targets of the kinome. In the present case, compounds targeting specific pathological MAPK/ERK and PI3K/AKT signaling states induced by different melanoma-relevant oncogenic mutations were identified. This approach measuring the activity of downstream proteins in signaling pathways has the potential to discover a diverse set of compounds that inhibit various upstream targets. With the advent of personalized medicine, it may be envisioned that once the genome of a patient tumor has been sequenced, specific compounds will be administered to the patient that will target the aberrant state depending on the specific oncogenic mutations.

Provided herein is a complementary and more targeted approach for the discovery of natural products with potential anticancer activity, as compared to standard approaches where cell survival, proliferation, or cytotoxicity is measured.[50−52] An important technical challenge was the cytotoxicity of extracts affecting cell morphology and, as a consequence, preventing measurement of meaningful ERK/AKT activities from biosensor images. For that purpose, a machine learning algorithm was developed to identify and exclude cells with altered morphology. This illustrates the challenges of image-based measurements of protein activity in HCS settings. Compounds targeting ERK/AKT activity may be overlooked if they are toxic at high concentrations or if they are present in extracts containing cytotoxic compounds.

The potential of the pipeline used is exemplified by the isolation of bioactive thymol derivatives from *A. montana* and piperamides from *P. nigrum*. However, the challenge of identifying the molecular target and the mechanism of action of active compounds remains. Promising approaches to address these issues include thermal proteome profiling, as well as protein and kinase microarrays.[53,54] While the most potent thymol derivative was active on both pathways at low micromolar concentrations, the piperamides showed only weak activity after isolation. This example illustrates the remaining challenge of selecting the most promising plants for scale-up isolation, given that the concentration of active compounds in an extract is unknown at that stage.

In summary, a proof of concept is provided of a scalable natural product screening and discovery pipeline to explore comprehensively the chemical space of extract libraries against the two key oncogenic pathways in melanoma. It is envisioned that this pipeline can be adapted to other molecular pathways and pathological conditions.

EXPERIMENTAL SECTION

General Experimental Procedures. Optical rotations were measured in MeOH (1 mg/mL) on a JASCO P-2000 polarimeter (Brechbühler AG, Switzerland) equipped with a 10 cm temperature-controlled microcell. ECD and UV spectra were recorded in MeOH (16.6−333.3 μg/mL) on a Chirascan CD spectrometer using 1 mm path precision cells (110 QS, Hellma Analytics). NMR spectra were recorded at 23 °C on a Bruker Avance III NMR spectrometer operating at 500.13 MHz for ^{1}H and 125.77 MHz for ^{13}C and equipped either with a 1 mm TXI microprobe or a 5 mm BBO probe. Spectra were recorded in $CDCl_3$ (Sigma-Aldrich/Merck), methanol-d_4, or DMSO-d_6 (both Armar Chemicals) and analyzed by Bruker TopSpin 3.5 and ACD/Laboratories NMR Workbook suite software. Chemical shifts are reported as δ values (ppm), with residual solvent signal as internal reference, J in Hz.

HPLC-grade solvents (Scharlau/Reuss Chemie/Macron) and ultrapure water from a Milli-Q water purification system (Merck Millipore) were used for analytical and semipreparative HPLC separations. HPLC-grade formic acid (FA), DMSO, and solvents were obtained from Scharlau or Macron Fine Chemicals. For extraction and preparative separation, technical-grade solvents were used after distillation. Accelerated solvent extraction (ASE) was performed using a ASE 200 extractor (Dionex). Normal-phase flash chromatography was carried out on a Puriflash 4100 (Interchim) or on a Sepacore system (Büchi), both consisting of a pump, UV detector, and fraction collector. Silica gel 60 (15−40 μm to pack column; 63−200 μm for dry loads of samples) was obtained from Merck. Preparative HPLC separations were carried out on a 1290 Infinity II Preparative LC/MS system (Agilent Technologies) consisting of a binary pump (1260 Prep Bin pump, 1290 Infinity II) connected to a PDA detector (1100 Series). Data acquisition and processing were performed with Chemstation (Agilent Technologies). A SunFire Prep C_{18} OBD column (5 μm, 30 × 150 mm i.d., Waters) equipped with a C_{18} Prep guard column (10 × 30 mm i.d.) was used at a flow rate of 20 mL/min.

Centrifugal partition chromatography (CPC) was performed on an Armen Spot centrifugal partition chromatography instrument (AlphaCrom) equipped with a ProStar 210 pump, a ProStar 325 UV/vis detector, and a ProStar 704 fraction collector (all Varian). Semipreparative HPLC was carried out on an HP 1100 Series system (Agilent Technologies) consisting of a binary pump, auto sampler, and diode array detector. Data acquisition and processing were performed using ChemStation software (Agilent Technologies). Semipreparative peak-based fractionation was performed with an Alliance 2690 HPLC system (Waters) equipped with a 996 diode array detector (Waters). Data acquisition and processing were performed using Empower software. The following columns were used: SunFire Prep C_{18} column (5 μm, 10 × 150 mm i.d., Waters) equipped with a guard column (10 × 10 mm i.d.), Xbridge Prep C_{18} (5 μm, 10 × 150 mm i.d., Waters) with a guard column (5 μm, 10 × 10 mm i.d.), Biphenyl Prep column (5 μm, 10 × 250 mm i.d., Kinetex).

HPLC-PDA-ELSD-ESIMS analyses were performed on an LC-MS 8030 system (Shimadzu) consisting of a degasser, binary high-pressure mixing pump, autosampler, column oven, and PDA detector. A triple quadrupole MS (LCMS-8030, Shimadzu) and an ELSD 3300 detector (Alltech) were connected via a T-splitter to the system. A SunFire C_{18} column (3.5 μm, 3 × 150 mm i.d., Waters) equipped with a C_{18} guard column (10 × 3 mm i.d.) was used at a flow rate of 0.4 mL/min.

TLC was performed on silica gel 60 F_{254} coated aluminum TLC plates (Merck). Detection was at UV 254 and 366 nm and after spraying with 1% ethanolic vanillin and 10% sulfuric acid in EtOH, followed by heating (10 min; 110 °C).

Plant Material. Roots of *Arnica montana* L. (Arnicae Radix) were purchased from Dixa AG (Switzerland) in two batches (lot nos. 181041 and 200968). A voucher specimen (1170) of lot no. 181041 is deposited at the Institute of Pharmaceutical Biology, University of Basel.

The dried fruits of *Piper nigrum* L. (Piperis Nigri Fructus) (lot no. 2008.04.0376) were purchased from Hänseler AG (Switzerland). A voucher specimen (no. 427) is deposited at the Institute of Pharmaceutical Biology, University of Basel.

Microfractionation and Activity Profiles. Microfractionation of the extracts was performed on an LC-MS 8030 system (Shimadzu) connected with an FC 204 fraction collector (Gilson). Extracts (10 mg/mL DMSO) were loaded in two portions (2 × 30 μL, corresponding to 0.6 mg of extract) on the analytical HPLC system. The separation was performed for 3 min at 10% CH_3CN, followed by a linear gradient to 100% CH_3CN over 27 min, and a final hold at 100% CH_3CN. The mobile phase contained 0.1% FA. A total of 24 microfractions of 1.5 min each (from 2 to 38 min) were collected into a 96-deepwell plate. Plates were dried overnight at 37 °C in an EZ-2 vacuum evaporator (Genevac). Dried residues were redissolved in DMSO and tested in the HCS assay.

Finally, one analytical HPLC trace was combined with the activity of fractions in R to generate the so-called HPLC time-based activity profiles.

https://doi.org/10.1021/acs.jnatprod.1c01154
J. Nat. Prod. 2022, 85, 1006−1017

Extraction and Isolation (*Arnica montana*). The material (lot no. 181041, 500 g) was ground and mixed with sea sand (2:1) prior to percolation. Extraction with 2.5 L of EtOAc afforded 12.4 g of dried extract.

The EtOAc extract was fractionated by flash chromatography on a silica column (45 × 7 cm). The sample was introduced as a dry load (12.4 g of extract absorbed on 36 g of silica gel). Elution was performed with a gradient of EtOAc in hexane [0% EtOAc (0−10 min), 0% → 5% (10−120 min), 5% → 20% (120−165 min), 20% (180 min), 20% → 100% (180−360 min) at a flow rate of 30 mL/min]. The column was further eluted with a gradient of MeOH in EtOAc [0 → 50% (360−390 min), 50% (390−420 min) at a flow rate of 30 mL/min]. Fractions (22 mL) were pooled to 11 main fractions (A−K) based on their TLC pattern.

Fraction H (1500 mg, 750 mg/mL THF) was submitted to preparative RP-HPLC with 50% CH_3CN (flow rate 20 mL/min) to afford two major fractions, H_B (449 mg, t_R 25 min) and H_D (65 mg, t_R 38 min). H_B (32 mg) was separated on a semipreparative RP-HPLC (XBridge C_{18}) with 35% CH_3CN (flow rate 4 mL/min) to afford compound **2** (12.3 mg, t_R 36 min). Fraction H_D (19 mg) was submitted to semipreparative RP-HPLC (Kinetex biphenyl) with 32% CH_3CN (flow rate of 5 mL/min) to afford compounds **3** (4.4 mg, t_R 75 min) and **4** (3.3 mg, t_R 80 min).

Fraction F (836 mg) was further fractionated on an open silica gel column (15 × 4 cm i.d.) using a step gradient of EtOAc−hexane [2:98 (2 L), 5:95 (1.7 L), 10:90 (1 L), 20:80 (0.5 L), 100:0 (0.6 L)]. Fractions (15 mL) were pooled to 21 main fractions (F_A−F_U) based on their TLC pattern. F_Q (53 mg) was submitted to semipreparative RP-HPLC (Sunfire C_{18} column) with 62% CH_3CN (containing 0.1% FA; flow rate of 4 mL/min) to afford compounds **6** (3.8 mg, t_R 63 min) and **7** (5.6 mg, t_R 68 min).

Fraction I (875 mg) was submitted to preparative RP-HPLC with a gradient method (15−100% CH_3CN in 30 min) to yield fraction I_B (57 mg, t_R 18 min). Fraction I_B (11 mg) was submitted to semipreparative RP-HPLC (Sunfire C_{18} column) with 22% CH_3CN (flow rate of 5 mL/min) to afford compound **1** (9.7 mg, t_R 16 min).

Ground material of lot no. 200968 (1000 g) was mixed with sea sand (2:1) for percolation. Extraction with 5 L of petroleum ether (PE) afforded 23.1 g of PE extract, and further extraction with 4 L of EtOAc yielded 7 g of EtOAc extract.

The PE extract of lot no. 200968 was fractionated by flash chromatography on a silica column (45 × 7 cm i.d.) with a Büchi Sepacore system. The sample was introduced as a dry load (23 g of extract absorbed on 60 g of silica gel). Elution was performed with a gradient of EtOAc in hexane [2% (0−45 min), 2% → 10% (45−120 min), 10% (120−205 min), 10% → 20% (205−265 min), 20% → 0% (265−505 min) at a flow rate of 30 mL/min]. The column was further eluted with MeOH in EtOAc [0% → 100% (505−535 min), 100% (535−545 min) at a flow rate of 30 mL/min]. Fractions (30 mL) were pooled to 25 main fractions (A−Y) based on their TLC pattern.

Fraction I (15 mg) was submitted to semipreparative RP-HPLC (Sunfire C_{18} column) with 35% CH_3CN (flow rate of 5 mL/min) to afford compound **5** (5 mg, t_R 44 min).

Extraction and Isolation (*Piper nigrum*). An aliquot (11.9 g) of ground fruits was extracted consecutively by ASE with dichloromethane and EtOAc (three extraction cycles each at 120 bar and 70 °C). The EtOAc extract afforded 94 mg of material. A peak-based collection of the extract (100 mg/mL DMSO) was done based on a previously reported method (Figure S38, Supporting Information).[42] The remaining part of the plant material (484 g) was mixed with sea sand for percolation. Extraction with 2 L of hexane afforded 10.6 g of dried extract, and a further extraction with EtOAc yielded 20.4 g of extract.

The EtOAc extract was separated on an open column with silica gel (63−200 μm, 55 × 6.5 cm i.d.), using a step gradient of PE−EtOAc (95:5, 90:10, 80:20, 70:30, 60:40 (each step 2 L), 50:50 (1 L), 40:60, 20:80, 0:100 (each step 2 L)). Fractions (220 mL) were pooled to 23 main fractions (F1−23) based on their TLC pattern. F15 (454 mg) and F16 (473 mg) were separated by CPC, utilizing a solvent system consisting of hexane−EtOAc−MeOH−H_2O (4:3:4:3). The pump was set to a flow rate of 5 mL/min and the rotor at 2000 rpm (333*g*). The instrument was run in the descending mode. Fractions were collected every 1.5 min for 70 min. The F15 fractions were pooled to nine (F15a−F15i) and F16 to five (F16a−F16e) main fractions, according to their UV absorbances.

Semipreparative RP-HPLC was used to further purify the following fractions with a Sunfire C_{18} column (flow rate 4 mL/min; 0.1% FA was added in all mobile phases, except for F16e). F15e (64 mg), F16e (94 mg), and a portion of F22 (2 g) were separated with 45% CH_3CN, 50% CH_3CN, and 40% CH_3CN, respectively, to obtain **11** (21 mg; t_R 32.5 min), **12** (31 mg, t_R 35.2), and **8** (9.5 mg; t_R 14.1 min). F21 (177 mg) was separated with a gradient of 40% to 85% CH_3CN over 30 min to obtain **10** (16 mg, t_R 20.4 min). Piperine (**9**) was identified with a reference substance (Sigma-Aldrich/Merck).

*8,10-Dihydroxy-9-isobutyryloxythymol (**1**):* colorless oil; $[\alpha]^{25}_D$ +6.8 (*c* 1 mg/mL, MeOH); UV (MeOH) λ_{max} (log ε) 199 (4.6), 217 (3.9), 277 (3.5) nm; ^1H and ^{13}C NMR, see Table S5, Supporting Information; ESIMS *m*/*z* 267 $[M - H]^-$

*8-Hydroxy-9,10-diisobutanoyloxythymol (**2**):* colorless oil; ^1H and ^{13}C NMR, see Table S5 and Figures S9 and S10, Supporting Information; ESIMS *m*/*z* 337 $[M - H]^-$.

*8-Hydroxy-9-isobutyryloxy-10-(2-methylbutanoyloxy)thymol (**3**):* colorless oil; $[\alpha]^{25}_D$ +15 (*c* 1 mg/mL, MeOH); UV (MeOH) λ_{max} (log ε) 199 (4.7), 217 (3.9), 273 (3.5) nm; ^1H and ^{13}C NMR, see Table S5, Supporting Information; ESIMS *m*/*z* 351 $[M - H]^-$.

*8-Hydroxy-9-isobutyryloxy-10-isopentanoyloxythymol (**4**):* colorless oil; ^1H and ^{13}C NMR, see Table S6, Supporting Information; ESIMS *m*/*z* 351 $[M - H]^-$.

*10-Isobutyryloxy-8,9-epoxythymol isobutyrate (**5**):* colorless oil; $[\alpha]^{25}_D$ +37 (*c* 1 mg/mL, MeOH); UV (MeOH) λ_{max} (log ε) 195 (5.2), 211 (4.5) nm; ^1H and ^{13}C NMR, see Table S6, Supporting Information; ESIMS *m*/*z* 321 $[M + H]^+$.

*10-(2-Methylbutyryloxy)-8,9-epoxythymol isobutyrate (**6**):* colorless oil; $[\alpha]^{25}_D$ +8.6 (*c* 1 mg/mL, MeOH); UV (MeOH) λ_{max} (log ε) 195 (4.0), 211 (3.4) nm; ^1H and ^{13}C NMR, see Table S6, Supporting Information; ESIMS *m*/*z* 335 $[M + H]^+$.

*10-Isopentanoyloxy-8,9-epoxythymol isobutyrate (**7**):* colorless oil; $[\alpha]^{25}_D$ +6.9 (*c* 1 mg/mL, MeOH); UV (MeOH) λ_{max} (log ε) 195 (3.8), 211 (3.2) nm; ^1H and ^{13}C NMR, see Table S6, Supporting Information; ESIMS *m*/*z* 335 $[M + H]^+$.

*Trichostachine (piperyline) (**8**):* pale yellow amorphous solid; ^1H and ^{13}C NMR, see Table S8, Supporting Information; ESIMS *m*/*z* 272 $[M + H]^+$.

*6,7-Dehydrobrachyamide B (**10**):* pale yellow amorphous solid; ^1H and ^{13}C NMR, see Table S8 and Figure S39, Supporting Information; ESIMS *m*/*z* 326 $[M + H]^+$.

*(2Z,4E,6E)-Piperettine (**11**):* yellow amorphous solid; ^1H and ^{13}C NMR, see Table S8, Supporting Information; ESIMS *m*/*z* 312 $[M + H]^+$.

*Piperolein A (**12**):* pale yellow amorphous solid; ^1H and ^{13}C NMR, see Table S8, Supporting Information; ESIMS *m*/*z* 316 $[M + H]^+$.

ECD Computational Methods. Conformational analysis was performed with Schrödinger MacroModel 11.0 (Schrödinger, LLC, New York, USA) employing the OPLS2005 (optimized potential for liquid simulations) force field in H_2O for geometrical optimization in two steps. In the first step, a global minimum was searched using 30 000 steps. In the second step, the global minimum was used for a conformational search (10 000−30 000 steps), and the five conformers with the lowest energy were subjected to geometrical optimization and energy calculation using density functional theory (DFT) at the B3LYP/6-31G(d,p) level of theory, using the SCRF method and the CPMC model for solvation in MeOH with the Gaussian 09 program package.[55] Excitation energy (denoted by wavelength in nm), rotator strength (R_{str}), dipole velocity (R_{vel}), and dipole length (R_{len}) were calculated in MeOH by TD-DFT (B3LYP/6-31G(d,p)). ECD curves were obtained on the basis of rotator strengths with a half-band of 0.25 eV using SpecDis v1.71.

High-Content Assay. Cells (100 μL) were seeded on 96-well black/clear flat-bottom plates (Falcon) at a density of 5000 cells/well

https://doi.org/10.1021/acs.jnatprod.1c01154
J. Nat. Prod. 2022, 85, 1006−1017

(A2058) and 4500 cells/well (MM121224), respectively. Cells were treated with samples 1 day after reseeding.

Sample Preparation. Samples to be tested were prepared for cell treatment as follows: Extracts (10 mg/mL in DMSO) were applied at a final concentration of 75 μg/mL. Microfractions (dry residues) were dissolved in either 5 or 10 μL of DMSO. The plates were shaken for 30 min at 500 rpm on a plate shaker (MixMate, Eppendorf). Complete RPMI medium was added to each fraction to obtain a DMSO concentration of 7.5%, and plates were shaken another 10 min. Finally, samples (10 μL) were added to each well. Isolated compounds were tested at eight different concentrations starting at 200 μM to 1.56 μM.

Cell Treatment with Samples. Extracts, fractions, and pure compounds were warmed in an incubator for 10 min prior to treatment. After application of treatment, plates were gently shaken manually for 1 min. Cells were incubated for 2 h, then fixed with PFA 4% [Sigma-Aldrich/Merck (36% PFA diluted with PBS)] for 10 min. MM121224 cells were washed three times with DPBS (Dutscher). A2058 cells were washed twice and stained with DAPI (1% in PBS) for 5 min followed by a third washing step.

The extract screen was performed in duplicate, with testing of pure compounds done in duplicate for *P. nigrum* and in triplicate for *A. montana*. For microfractions only single experiments were performed.

Positive controls for A2058 cells were 20 μM AZD5363 (Selleckchem) as AKT inhibitor and 500 nM cobimetinib (Selleckchem) as ERK pathway inhibitor. For MM121224 cells, 200 nM cobimetinib as ERK pathway inhibitor and 1 μM GDC0941 (Selleckchem) as AKT pathway inhibitor were used. The negative control was 0.75% DMSO in complete medium.

Cell Lines and Cell Culture. A2058 cells (ATTC-CRL-11147) were cultured in DMEM growth medium (Sigma-Aldrich/Merck) supplemented with 10% fetal bovine serum (FBS, Good Forte by PAN Biotech), 1% penicillin/streptomycin (ThermoFisher), and 2% glutamine (Biowest). Patient-derived MM121224 cells[26] were cultured in RPMI growth medium (Sigma-Aldrich/Merck), 10% FBS (Good Forte by PAN Biotech), 1% penicillin/streptomycin (ThermoFisher), and 1% sodium pyruvate (Sigma-Aldrich/Merck). Both cell lines were incubated in humidified air at 37 °C and 5% CO_2. Cells were passaged at 70−80% confluence using trypsin-EDTA (Sigma). Passage numbers used were 20−40 for A2058 and 17−28 for MM121224. The cell lines were regularly tested for mycoplasma contamination with MycoAlert (Lonza).

Plasmids. A2058 cells were transfected to stably express H2B-miRFP703, ERK-KTR-mScarlet, and FoxO3a-KTR-mNeonGreen. MM121224 cells were transfected to stably express H2B-mTurquoise, ERK-KTR-mScarlet, and FoxO3a-KTR-mNeonGreen. Both cell lines were generated by transfection with FuGENE (Promega) according to the manufacturer's protocol and antibiotic selection with blasticidin, hygromycin, and puromycin, respectively. As previously described, the H2B-miRFP703 and H2B-mTurquoiose nuclear markers were constructed by fusing the coding sequences (CDS) of human H2B clustered histone 11 (H2BC11) with the fluorescent protein miRFP703 and mTurquoise CDS, respectively.[56] The nuclear marker was then cloned into PiggyBac plasmid pPBbSr2-MCS. ERK-KTR-mScarlet was constructed by fusing ERK-KTR CDS[57] with the fluorescent protein mScarlet CDS and cloning it into the PiggyBac plasmid pBr-HPB. FoxO3a-KTR (AKT-KTR) was generated by fusing the 1-1188 portion of the *Homo sapiens* forkhead box O3 a (FoxO3a) CDS with the fluorescent protein mNeonGreen CDS and cloned into PiggyBac plasmid pSB-HPB. The Super Piggybac transposase expression vector was used for cotransfection with the PiggyBac plasmids in order to facilitate integration at TTAA sites.[58]

Immunostaining. Wild-type MM121224 cells were fixed in 4% PFA and washed 3 × 5 min with PBS. Cells were permeabilized for 20 min with 0.1% Triton X-100 (PanReac AppliChem ITW Reagents) in PBS and washed 3 × 5 min with PBS. Blocking was performed with 2% BSA and 22.52 mg/mL glycine in PBST (PBS + 0.1% Tween 20) for 40 min and washed once with PBS; then cells were incubated with primary antibodies (monoclonal anti-MAP kinase, activated (diphosphorylated ERK-1&2, Sigma-Aldrich; Phospho-Akt (Ser473), Cell Signaling Technology) in 0.1% bovine serum albumin (BSA) in PBST overnight at 4 °C. The day after, cells were washed 3 × 5 min with PBS and incubated with secondary antibodies (Alexa 546 goat anti-mouse and Alexa 546 goat anti-mouse; both Life Technolgies/ThermoFisher) in 0.1% BSA in PBST for 1 h at room temperature. Cells were washed 3 × 5 min, counterstained with DAPI for 5 min, and washed two times with PBS. Cells were then imaged.

Imaging. All imaging experiments except immunostainings were performed on an Operetta HCS microscope (widefield and spinning disk, xenon arc lamp 200 W) equipped with a CCD camera and a plate handler robot. Images were acquired using a 10× LWD objective (NA: 0.3; working distance 10 mm). Acquisition channels were set as follows: mScarlett (ERK-KTR) 560−580 nm (excitation), 590−640 nm (emission); neongreen (AKT-KTR) 490−510 nm (excitation), 520−560 nm (emission); mTurquoise (H2B) 410−430 nm (excitation), 460−500 nm (emission); DAPI: 360−400 nm (excitation), 410−480 nm (emission). For each well 15 images (fields of view) per channel were acquired.

Immunostaining experiments were imaged with an Eclipse Ti inverted fluorescence microscope (Nikon) run by NIS-Elements (Nikon) and equipped with a Plan Apo air 20× (NA 0.8) and an Andor Zyla 4.2 plus camera (16-bit depth images). Focus drift was prevented by the Perfect Focus System (Nikon). The optical configurations of the acquisition channels were the following (all filters from Chroma): Alexa 546: 555 nm, ET605/52m; Alexa488: 470 nm, ET525/36m; DAPI: 410 nm, ET460/50m.

Image Analysis. Images were processed with CellProfiler 2.3.1 software (Broad Institute). The threshold-based segmentation algorithm identified nuclei in the mTurquoise/DAPI channel. To measure fluorescence intensity in the nucleus, the nuclear mask was reduced by two pixels to exclude blurred edges of the nucleus. To measure fluorescence intensity in the cytosol, a ring was created around the nucleus. First, the nuclear mask was expanded by maximum 15 pixels by thresholding the sum of ERK and AKT channels. Then, this new mask was subtracted from the nuclear mask expanded by two pixels to exclude blurred edges of the nucleus. The resulting ring was used to measure fluorescence in the cytosol. Single-cell ERK and AKT activity was estimated by taking the ratio of the cytosolic and nuclear mean fluorescence intensities (i.e., the C/N ratio). The shape features of individual cells were calculated from a whole-cell segmentation (nuclear mask expanded by a maximum 100 pixels) on the sum of ERK and AKT channels.

Data Analysis. The data were processed with custom scripts written in R programming language. Cells dying due to cytotoxicity gave rise to false positive hits and thus became the main target of the filtering step. To remove them from the analysis, a random-forest model implemented in the H2O.ai machine-learning framework was trained. The models were trained to separate healthy from dying cells based on fluorescence intensity and shape features of single cells. The prediction accuracy was 98% for the model trained on the A2058 cell line and 94% for the MM121224 model. Additionally, (i) cells with C/N ratios greater than 5, (ii) fields of view with less than 15% living cells, and (iii) wells with less than five viable fields of view or with less than 200 living cells were discarded.

Plates were normalized by calculating normalized percentage inhibition and *z*-score. The NPI rescales the C/N ratio between the means of the negative and positive controls. For this purpose, it was assumed that NPI = 1 corresponds to the negative and NPI = 0 to the positive control. The *z*-score is the number of standard deviations a sample is away from the plate mean (excluding the control wells).

Z' was calculated to assess plate quality. This value quantifies the distance between the distributions of negative and positive controls.[59] $Z' = 1$ is the theoretical limit for an ideal screen with no variability in controls or the dynamic range reaching infinity. A Z' between 0.5 and 1 corresponds to a plate with a large separation band between controls. The screen typically achieved a Z' between 0.55 and 0.92.

Data Visualization. An interactive web application, dzPlateViewer, was developed to quickly browse raw images from the entire plate and the accompanying quantification. Users were able to switch between the channels (e.g., nuclear, ERK, AKT), adjust image

https://doi.org/10.1021/acs.jnatprod.1c01154
J. Nat. Prod. 2022, 85, 1006−1017

brightness, contrast, and levels, and browse an interactive heatmap with C/N ratios, NPI, or a *z*-score. Also available were violin plots to visualize the distribution of samples and controls. The portal was developed in Python/HTML/JavaScript and took advantage of the OpenSeadragon framework and Python Deep Zoom Tools. The code for the portal is open source and available at https://github.com/dmattek/dzPlateViewer.

■ ASSOCIATED CONTENT

Supporting Information

The Supporting Information is available free of charge at https://pubs.acs.org/doi/10.1021/acs.jnatprod.1c01154.

Additional details on assay with pathways in cell and plate viewer, hit lists, additional HPLC-based activity profiles, NMR spectra for all compounds, calculated and experimental ECD and UV spectra for **1**−**7**, and concentration−response curve of all compounds (PDF)

■ AUTHOR INFORMATION

Corresponding Author

Eliane Garo − *Division of Pharmaceutical Biology, Department of Pharmaceutical Sciences, University of Basel, 4056 Basel, Switzerland;* orcid.org/0000-0002-3497-2524; Email: eliane.garo@unibas.ch

Authors

Lara Dürr − *Division of Pharmaceutical Biology, Department of Pharmaceutical Sciences, University of Basel, 4056 Basel, Switzerland*

Tanja Hell − *Division of Pharmaceutical Biology, Department of Pharmaceutical Sciences, University of Basel, 4056 Basel, Switzerland;* orcid.org/0000-0002-8867-2412

Maciej Dobrzyński − *Institute of Cell Biology, University of Bern, 3012 Bern, Switzerland*

Alberto Mattei − *Institute of Cell Biology, University of Bern, 3012 Bern, Switzerland*

Anika John − *Institute of Cell Biology, University of Bern, 3012 Bern, Switzerland*

Nathanja Augsburger − *Division of Pharmaceutical Biology, Department of Pharmaceutical Sciences, University of Basel, 4056 Basel, Switzerland*

Gloria Bradanini − *Division of Pharmaceutical Biology, Department of Pharmaceutical Sciences, University of Basel, 4056 Basel, Switzerland*

Jakob K. Reinhardt − *Division of Pharmaceutical Biology, Department of Pharmaceutical Sciences, University of Basel, 4056 Basel, Switzerland;* orcid.org/0000-0002-8675-1029

Florian Rossberg − *Division of Pharmaceutical Biology, Department of Pharmaceutical Sciences, University of Basel, 4056 Basel, Switzerland*

Milos Drobnjakovic − *Institute of Cell Biology, University of Bern, 3012 Bern, Switzerland*

▽**Mahabir P. Gupta** − *Center for Pharmacognostic Research and Panamanian Flora, Faculty of Pharmacy, University of Panama, Panama City 0801, Republic of Panama*

Matthias Hamburger − *Division of Pharmaceutical Biology, Department of Pharmaceutical Sciences, University of Basel, 4056 Basel, Switzerland;* orcid.org/0000-0001-9331-273X

Olivier Pertz − *Institute of Cell Biology, University of Bern, 3012 Bern, Switzerland;* orcid.org/0000-0001-8579-4919

Complete contact information is available at: https://pubs.acs.org/10.1021/acs.jnatprod.1c01154

Author Contributions

‡L.D. and T.H. contributed equally.

Notes

The authors declare no competing financial interest.

▽Deceased on December 14, 2020.

■ ACKNOWLEDGMENTS

We thank Mitchell Levesque (University Hospital of Zurich) for providing the MM121224 cell line and Matthias Wymann (Department of Biomedicine, University of Basel) for the A2058 cell line. We are grateful to the DBM Microscopy Core Facility (Department of Biomedicine, University of Basel), especially Pascal Lorentz, for access to the HCS microscope and for technical support. We acknowledge Alex Espinosa, botanist at CIFLORPAN, for identification of the Panamanian plants. ECD spectra were measured at the Biophysics Facility, Biozentrum, University of Basel. Funding was provided by grants (205321-176008) from the Swiss National Science Foundation (to M.H. and O.P.) and from the Swiss Cancer League (KFS-3727-08-2015; O.P.).

■ REFERENCES

(1) Matthews, N. H.; Li, W.-Q.; Qureshi, A. A.; Weinstock, M. A.; Cho, E. In *Cutaneous Melanoma: Etiology and Therapy*; Ward, W. H.; Farma, J. M., Eds.; Codon Publications: Brisbane, 2017; pp 3−22.

(2) Yajima, I.; Kumasaka, M. Y.; Thang, N. D.; Goto, Y.; Takeda, K.; Yamanoshita, O.; Iida, M.; Ohgami, N.; Tamura, H.; Kawamoto, Y.; Kato, M. *Dermatol. Res. Pract.* **2012**, *2012*, 354191.

(3) Tanda, E. T.; Vanni, I.; Boutros, A.; Andreotti, V.; Bruno, W.; Ghiorzo, P.; Spagnolo, F. *Front. Mol. Biosci.* **2020**, *7*, 154.

(4) Van Allen, E. M.; Wagle, N.; Sucker, A.; Treacy, D. J.; Johannessen, C. M.; Goetz, E. M.; Place, C. S.; Taylor-Weiner, A.; Whittaker, S.; Kryukov, G. V.; Hodis, E.; Rosenberg, M.; McKenna, A.; Cibulskis, K.; Farlow, D.; Zimmer, L.; Hillen, U.; Gutzmer, R.; Goldinger, S. M.; Ugurel, S.; Gogas, H. J.; Egberts, F.; Berking, C.; Trefzer, U.; Loquai, C.; Weide, B.; Hassel, J. C.; Gabriel, S. B.; Carter, S. L.; Getz, G.; Garraway, L. A.; Schadendorf, D. *Cancer Discovery* **2014**, *4*, 94−109.

(5) Arozarena, I.; Wellbrock, C. *Ann. Transl. Med.* **2017**, *5*, 387.

(6) Shi, H.; Hugo, W.; Kong, X.; Hong, A.; Koya, R. C.; Moriceau, G.; Chodon, T.; Guo, R.; Johnson, D. B.; Dahlman, K. B.; Kelley, M. C.; Kefford, R. F.; Chmielowski, B.; Glaspy, J. A.; Sosman, J. A.; van Baren, N.; Long, G. V.; Ribas, A.; Lo, R. S. *Cancer Discovery* **2014**, *4*, 80−93.

(7) Vu, H. L.; Aplin, A. E. *Pharmacol. Res.* **2016**, *107*, 111−116.

(8) Dantonio, P. M.; Klein, M. O.; Freire, M. R. V. B.; Araujo, C. N.; Chiacetti, A. C.; Correa, R. G. *Biosci. Rep.* **2018**, *38*, 15−21.

(9) Eroglu, Z.; Ribas, A. *Ther. Adv. Med. Oncol.* **2016**, *8*, 48−56.

(10) Lim, S. Y.; Menzies, A. M.; Rizos, H. *Cancer* **2017**, *123*, 2118−2129.

(11) Cao, Z.; Liao, Q.; Su, M.; Huang, K.; Jin, J.; Cao, D. *Cancer Lett.* **2019**, *459*, 30−40.

(12) Wagner, J.; Kline, C. L.; Ralff, M. D.; Lev, A.; Lulla, A.; Zhou, L.; Olson, G. L.; Nallaganchu, B. R.; Benes, C. H.; Allen, J. E.; Prabhu, V. V.; Stogniew, M.; Oster, W.; El-Deiry, W. S. *Cell Cycle* **2017**, *16*, 1790−1799.

(13) Satyamoorthy, K.; Li, G.; Gerrero, M. R.; Brose, M. S.; Volpe, P.; Weber, B. L.; van Belle, P.; Elder, D. E.; Herlyn, M. *Cancer Res.* **2003**, *63*, 756−759.

(14) Karasarides, M.; Chiloeches, A.; Hayward, R.; Niculescu-Duvaz, D.; Scanlon, I.; Friedlos, F.; Ogilvie, L.; Hedley, D.; Martin, J.; Marshall, C. J.; Springer, C. J.; Marais, R. *Oncogene* **2004**, *23*, 6292−6298.
(15) Hingorani, S. R.; Jacobetz, M. A.; Robertson, G. P.; Herlyn, M.; Tuveson, D. A. *Cancer Res.* **2003**, *63*, 5198−5202.
(16) Hoeflich, K. P.; Gray, D. C.; Eby, M. T.; Tien, J. Y.; Wong, L.; Bower, J.; Gogineni, A.; Zha, J.; Cole, M. J.; Stern, H. M.; Murray, L. J.; Davis, D. P.; Seshagiri, S. *Cancer Res.* **2006**, *66*, 999−1006.
(17) Wan, P. T. C.; Garnett, M. J.; Roe, S. M.; Lee, S.; Niculescu-Duvaz, D.; Good, V. M.; Project, C. G.; Jones, C. M.; Marshall, C. J.; Springer, C. J.; Barford, D.; Marais, R. *Cell* **2004**, *116*, 855−867.
(18) Bollag, G.; Tsai, J.; Zhang, J.; Zhang, C.; Ibrahim, P.; Nolop, K.; Hirth, P. *Nat. Rev. Drug Discovery* **2012**, *11*, 873−886.
(19) Regot, S.; Hughey, J. J.; Bajar, B. T.; Carrasco, S.; Covert, M. *Cell* **2014**, *157*, 1724−1734.
(20) Klinger, B.; Blüthgen, N. *Biochem. Soc. Trans.* **2014**, *42*, 770−775.
(21) Lito, P.; Rosen, N.; Solit, D. B. *Nat. Med.* **2013**, *19*, 1401−1409.
(22) Potterat, O.; Hamburger, M. *Planta Med.* **2014**, *80*, 1171−1181.
(23) Bindels, D. S.; Haarbosch, L.; van Weeren, L.; Postma, M.; Wiese, K. E.; Mastop, M.; Aumonier, S.; Gotthard, G.; Royant, A.; Hink, M. A.; Gadella, T. W. J. *Nat. Methods* **2017**, *14*, 53−56.
(24) Shaner, N. C.; Lambert, G. G.; Chammas, A.; Ni, Y.; Cranfill, P. J.; Baird, M. A.; Sell, B. R.; Allen, J. R.; Day, R. N.; Israelsson, M.; Davidson, M. W.; Wang, J. *Nat. Methods* **2013**, *10*, 407−409.
(25) Mattei, A. *Exploring Signaling Mechanisms Regulating Genetic and Non-genetic Drug Resistance in Melanoma*; Ph.D. Dissertation, University of Bern, 2021.
(26) Raaijmakers, M. I. G.; Widmer, D. S.; Narechania, A.; Eichhoff, O.; Freiberger, S. N.; Wenzina, J.; Cheng, P. F.; Mihic-Probst, D.; Desalle, R.; Dummer, R.; Levesque, M. P. *Oncotarget* **2016**, *7*, 77163−77174.
(27) Gerosa, L.; Chidley, C.; Fröhlich, F.; Sanchez, G.; Lim, S. K.; Muhlich, J.; Chen, J.-Y.; Vallabhaneni, S.; Baker, G. J.; Schapiro, D.; Atanasova, M. I.; Chylek, L. A.; Shi, T.; Yi, L.; Nicora, C. D.; Claas, A.; Ng, T. S. C.; Kohler, R. H.; Lauffenburger, D. A.; Weissleder, R.; Miller, M. A.; Qian, W.-J.; Wiley, H. S.; Sorger, P. K. *Cell Syst.* **2020**, *11*, 478−494.e9.
(28) Lito, P.; Pratilas, C. A.; Joseph, E. W.; Tadi, M.; Halilovic, E.; Zubrowski, M.; Huang, A.; Wong, W. L.; Callahan, M. K.; Merghoub, T.; Wolchok, J. D.; de Stanchina, E.; Chandarlapaty, S.; Poulikakos, P. I.; Fagin, J. A.; Rosen, N. *Cancer Cell* **2012**, *22*, 668−682.
(29) Dessauges, C.; Mikelson, J.; Dobrzyński, M.; Jacques, M.-A.; Frismantiene, A.; Gagliardi, P. A.; Khammash, M.; Pertz, O. *bioRxiv* **2021**, DOI: 10.1101/2021.07.27.453955.
(30) Pratilas, C. A.; Taylor, B. S.; Ye, Q.; Viale, A.; Sander, C.; Solit, D. B.; Rosen, N. *Proc. Natl. Acad. Sci. U. S. A.* **2009**, *106*, 4519−4524.
(31) Trang, N. D.; Wanner, M. J.; Koomen, G.-J.; Dung, N. X. *Planta Med.* **1993**, *59*, 480−481.
(32) Mossa, J. S.; El-Feraly, F. S.; Muhammad, I.; Zaw, K.; Mbwambo, Z. H.; Pezzuto, J. M.; Fong, H. H. S. *J. Nat. Prod.* **1997**, *60*, 550−555.
(33) Su, B.-N.; Takaishi, Y.; Yabuuchi, T.; Kusumi, T.; Tori, M.; Takaoka, S.; Honda, G.; Ito, M.; Takeda, Y.; Kodzhimatov, O. K.; Ashurmetov, O. *J. Nat. Prod.* **2001**, *64*, 466−471.
(34) Kłeczek, N.; Malarz, J.; Kosecka-Strojek, M.; Musielak, B.; Stojakowska, A. *Phytochem. Lett.* **2019**, *30*, 235−237.
(35) Bohlmann, F.; Jakupovic, J.; King, R. M.; Robinson, H. *Phytochemistry* **1982**, *21*, 1103−1107.
(36) Arreaga-González, H. M.; Pardo-Novoa, J. C.; del Río, R. E.; Rodríguez-García, G.; Torres-Valencia, J. M.; Manríquez-Torres, J. J.; Cerda-García-Rojas, C. M.; Joseph-Nathan, P.; Gómez-Hurtado, M. A. *J. Nat. Prod.* **2018**, *81*, 63−71.
(37) Weremczuk-Jeżyna, I.; Kisiel, W.; Wysokińska, H. *Plant Cell Rep.* **2006**, *25*, 993−996.
(38) Hong, M. J.; Kim, J. *J. Nat. Prod.* **2017**, *80*, 1354−1360.
(39) Qiu, S.-X.; Lin, L.-Z.; Nan, Y.; Lin, P.; Chen, J.-J.; Zhang, Z.-X.; Zhou, J.; Cordell, G. A. *Phytochemistry* **1995**, *40*, 917−921.
(40) Lv, R.; Chen, Z. *Trop. J. Pharm. Res.* **2018**, *16*, 2895−2901.
(41) Birtwistle, M. R.; Kolch, W. *Cell Cycle Georget. Tex.* **2011**, *10*, 2069−2076.
(42) Zaugg, J.; Baburin, I.; Strommer, B.; Kim, H.-J.; Hering, S.; Hamburger, M. *J. Nat. Prod.* **2010**, *73*, 185−191.
(43) Olsen, R. A.; Spessard, G. O. *J. Agric. Food Chem.* **1981**, *29*, 942−944.
(44) Wei, K.; Li, W.; Koike, K.; Pei, Y.; Chen, Y.; Nikaido, T. *J. Nat. Prod.* **2004**, *67*, 1005−1009.
(45) Kiuchi, F.; Nakamura, N.; Saitoh, M.; Komagome, K.; Hiramatsu, H.; Takimoto, N.; Akao, N.; Kondo, K.; Tsuda, Y. *Chem. Pharm. Bull.* **1997**, *45*, 685−696.
(46) Friedman, M.; Levin, C. E.; Lee, S.-U.; Lee, J.-S.; Ohnisi-Kameyama, M.; Kozukue, N. *J. Agric. Food Chem.* **2008**, *56*, 3028−3036.
(47) Strunz, G. M.; Finlay, H. *Tetrahedron* **1994**, *50*, 11113−11122.
(48) Zeng, Y.; Yang, Y. *Mol. Med. Rep.* **2018**, *17*, 6363−6370.
(49) Hwang, Y. P.; Yun, H. J.; Kim, H. G.; Han, E. H.; Choi, J. H.; Chung, Y. C.; Jeong, H. G. *Toxicol. Lett.* **2011**, *203*, 9−19.
(50) Harvey, A. L.; Cree, I. A. *Planta Med.* **2010**, *76*, 1080−1086.
(51) Shoemaker, R. H. *Nat. Rev. Cancer* **2006**, *6*, 813−823.
(52) Wilson, B. A. P.; Thornburg, C. C.; Henrich, C. J.; Grkovic, T.; O'Keefe, B. R. *Nat. Prod. Rep.* **2020**, *37*, 893−918.
(53) Savitski, M. M.; Reinhard, F. B. M.; Franken, H.; Werner, T.; Savitski, M. F.; Eberhard, D.; Martinez Molina, D.; Jafari, R.; Dovega, R. B.; Klaeger, S.; Kuster, B.; Nordlund, P.; Bantscheff, M.; Drewes, G. *Science* **2014**, *346*, 1255784.
(54) Duarte, J. G.; Blackburn, J. M. *Expert Rev. Proteomics* **2017**, *14*, 627−641.
(55) Frisch, M. J.; Trucks, G. W.; Schlegel, H. B.; Scuseria, G. E.; Robb, M. A.; Cheeseman, J. R.; Scalmani, G.; Barone, V.; Petersson, G. A.; Nakatsuji, H.; Li, X.; Caricato, M.; Marenich, A.; Bloino, J.; Janesko, B. G.; Gomperts, R.; Mennucci, B.; Hratchian, H. P.; Ortiz, J. V.; Izmaylov, A. F.; Sonnenberg, J. L.; Williams-Young, D.; Ding, F.; Lipparini, F.; Egidi, F.; Goings, J.; Peng, B.; Petrone, A.; Henderson, T.; Ranasinghe, D.; Zakrzewski, V. G.; Gao, J.; Rega, N.; Zheng, G.; Liang, W.; Hada, M.; Ehara, M.; Toyota, K.; Fukuda, R.; Hasegawa, J.; Ishida, M.; Nakajima, T.; Honda, Y.; Kitao, O.; Naka, H.; Vreven, T.; Throssell, K.; Montgomery, J. A.; Peralta, J. E.; Ogliaro, F.; Bearpark, M.; Heyd, J. J.; Brothers, E.; Kudin, K. N.; Staroverov, V. N.; Keith, T.; Kobayashi, R.; Normand, J.; Raghavachari, K.; Rendel, A.; Burant, J. C.; Iyengar, S. S.; Tomasi, J.; Cossi, M.; Millam, J. M.; Klene, M.; Adamo, C.; Cammi, R.; Ochterski, J. W.; Martin, R. L.; Morokuma, K.; Farkas, O.; Foresman, J. B.; Fox, D. J. *Gaussian 09, Revision D.01*; Gaussian Inc.: Wallingford, CT, 2009.
(56) Gagliardi, P. A.; Dobrzyński, M.; Jacques, M.-A.; Dessauges, C.; Ender, P.; Blum, Y.; Hughes, R. M.; Cohen, A. R.; Pertz, O. *Dev. Cell* **2021**, *56*, 1712−1726.e6.
(57) Regot, S.; Hughey, J. J.; Bajar, B. T.; Carrasco, S.; Covert, M. W. *Cell* **2014**, *157*, 1724−1734.
(58) Suzuki, S.; Tsukiyama, T.; Kaneko, T.; Imai, H.; Minami, N. *J. Reprod. Dev.* **2015**, *61*, 241−244.
(59) Zhang, J.-H.; Chung, T. D. Y.; Oldenburg, K. R. *J. Biomol. Screen.* **1999**, *4*, 67−73.

https://doi.org/10.1021/acs.jnatprod.1c01154
J. Nat. Prod. 2022, 85, 1006−1017